Acta Materialia 264 (2024) 119552

Contents lists available at ScienceDirect

Acta Materialia

journal homepage: www.elsevier.com/locate/actamat

Full length article

Modelling the spatial evolution of excess vacancies and its influence on age hardening behaviors in multicomponent aluminium alloys

Xuezhou Wang [a], Dongdong Zhao [a,b], Yijiang Xu [c], Yanjun Li [a,*]

[a] Department of Materials Science and Engineering, Norwegian University of Science and Technology, 7491 Trondheim, Norway
[b] School of Materials Science and Engineering and Tianjin Key Laboratory of Composite and Functional Materials, Tianjin University, Tianjin 300350, China
[c] SINTEF Industry, 7465 Trondheim, Norway

ARTICLE INFO

Keywords:
Aluminium alloys
Ageing
Vacancies
Annihilation
Precipitation kinetics

ABSTRACT

Excess vacancies play crucial roles in the precipitation of age-hardening precipitates in aluminium alloys, but their spatial evolution across grains during heat treatments is less known. In this work, a numerical model is developed to predict the spatial evolution of non-equilibrium excess vacancies during cooling from solution treatment and during ageing heat treatments of multicomponent aluminium alloys. A finite volume scheme is applied to derive the spatial distribution of vacancy site fraction across grains by solving the diffusion equations of vacancies under the influence of solute elements. Binding energies between solute atoms and vacancies predicted by first-principles calculations has been used to handle the trapping of excess vacancies by solute atoms and atom clusters. The annihilation rates of excess vacancies at grain boundaries and at dislocation jogs have been derived based on a rigorous description of the annihilation mechanisms of vacancies. The evolution of the density of dislocation jogs due to vacancy annihilation has been taken into account. The model is successfully applied to interpret the age hardening behaviors of experimental alloys subjected to different thermomechanical processing conditions. This model will help to reach a deeper understanding of the roles of excess vacancies in precipitation kinetics and therefore is important to further optimize thermomechanical processing parameters and alloy composition to improve the macroscopic mechanical properties of age hardening aluminium alloys.

1. Introduction

Excess vacancies in aluminium alloys induced by rapid quenching from solution treatment [1–3] or plastic deformation [4,5] have strong influences on the solute diffusion, atom clustering, grain boundary segregation and therefore the precipitation behavior of age hardening precipitates [6–8]. Specifically, excess vacancies reduce the energy barrier for nucleation of precipitates by releasing the misfit strain of the nucleus. They can also increase the diffusivity of substitutional solute atoms through vacancy-exchange mechanisms [9–12]. Moreover, the annihilation of excess vacancies at grain boundaries (GBs) has long been considered as one of the important reasons for the formation of precipitate-free zones (PFZs) near GBs in aluminium alloys [13,14], which leads to localization of plastic strain and induces the nucleation of microcracks during deformation [15–17]. In light of this, it is of great importance to understand the annihilation kinetics of excess vacancies at different sinks and their spatial distribution and evolution across grains during cooling from solution treatment and during ageing heat treatments at different temperatures.

Vacancy is difficult to measure directly by any experimental approaches available. So far, positron annihilation lifetime spectroscopy (PALS) is the most powerful method to evaluate the concentration of vacancies [18]. It has been successfully applied in pure aluminium [19]. However, vacancies can exist in different states, i.e., mono vacancy, bound with different solute atoms or atoms clusters in multicomponent alloys, which leads to different lifetimes of positrons trapped in those vacancies. As a consequence, only approximate vacancy concentration values can be obtained by fitting the measured positron lifetime since the various contributions cannot be clearly distinguished [5,20]. Therefore, a rigorous physics-based model is desired to quantitatively study the annihilation behaviors of excess vacancies during age hardening of aluminium alloys.

In the last decades, many research efforts have been spent to develop numerical models to predict the evolution of excess vacancies and its influence on precipitation behavior at various temperatures. Militzer et al. [21] proposed a phenomenological model to simulate the time

* Corresponding author.
E-mail address: yanjun.li@ntnu.no (Y. Li).

https://doi.org/10.1016/j.actamat.2023.119552
Received 30 June 2023; Received in revised form 21 November 2023; Accepted 25 November 2023
Available online 26 November 2023

evolution of excess vacancies during and after high-temperature deformation ($T > 0.4T_m$), in which both the generation and annihilation of vacancies were taken into account. In the model, the annihilation of excess vacancies was considered to take place at dislocation lines and at GBs of cubic grains controlled by quasi-steady state diffusion. This analytical model was recently applied by Robson [22] to quantitatively explore the effects of excess vacancies and dislocations generated by the deformation at different strain rates and temperatures on the diffusion behaviors of solute species in aluminium alloys. Fischer et al. [23] developed a kinetic model to predict the annihilation rates of vacancies at grain boundaries, dislocation jogs and unstable Frank loops during ageing heat treatments, based on a non-equilibrium Onsager's thermodynamics concept [24–27]. In the model, the dislocation jogs were treated as independent vacancy sinks homogeneously distributed in the grain interior with a constant density, and the site fraction of vacancies was assumed to be spatially constant across grains. Francis and Curtin [28] developed a generalized thermodynamic model to assess the influences of repartitioning of vacancies between bulk lattice sites and the sites neighboring the minutely added solutes on the precipitation kinetics during ageing treatments in metal alloys [29,30]. In the model, the annihilation of quenched-in excess vacancies at different sinks was neglected below an effective solution temperature. Recently, Yang et al. [20] described a physics-based model to investigate the effect of quenched-in excess vacancies on natural and artificial ageing in an Al-Mg-Si alloy by simultaneously considering the influences of annihilation, trapping and repartitioning of excess vacancies on the precipitation behavior, following the same vacancy annihilation mechanisms proposed by Fischer et al. [23]. However, the above models either i) estimated the annihilation rate of vacancies at GBs based on quasi-steady state diffusion [21,22] or ii) assumed spatially uniform distribution of vacancies across grains [20,23,28] during ageing heat treatments. As a consequence, the transient spatial distribution of vacancies vicinal to the GBs could not be predicted by the above models, which is essential to understand the formation mechanisms of PFZ. Furthermore, the assumptions of homogeneous distribution and constant dislocation jog density may cause an overestimation of the vacancy annihilation rate, because the jog density changes with temperature and vacancy supersaturation [31] and therefore alters the annihilation rate of excess vacancies [32].

To meet the challenges existing in the previous models, a numerical model has been developed in this work to predict the spatial evolution of excess vacancies across grains of age hardening aluminium alloys during cooling from solution treatment and during ageing at different temperatures. In the model, to well address the diffusion of vacancies within grains, a finite volume method is applied. Instead of assuming homogeneous distribution and constant density in the grain, the dislocation jogs are located along dislocation lines as point defects and their density changes due to vacancy annihilation. The trapping effect of solute elements on vacancies is also rigorously described. The rest of the present paper is organized as follows. Section 2 describes the numerical model. In Section 3, the model is evaluated in comparison to a previous analytical model [23]. In Section 4, the model is applied to a couple of experimental alloys showing the influences of temperature history, grain size, dislocation density and alloy chemistry on vacancy evolution and therefore on the precipitation behavior of age hardening precipitates. Finally, the simulation results are discussed in Section 5 and a conclusive remark is presented in Section 6.

2. Model description

The GBs, as well as free surfaces and dislocation jogs, are effective sinks for excess vacancies to be annihilated [23]. The Frank loops are neglected in this work since they are more favorable to form in high-purity Al quenched from a lower solution temperature with a lower cooling rate, and may dissolve very rapidly and are therefore unstable [33,34]. All kinds of sinks are considered to be ideal, which means that the site fraction of vacancies at these sinks can instantaneously reach the equilibrium value at certain temperatures $T(t)$, i.e.,

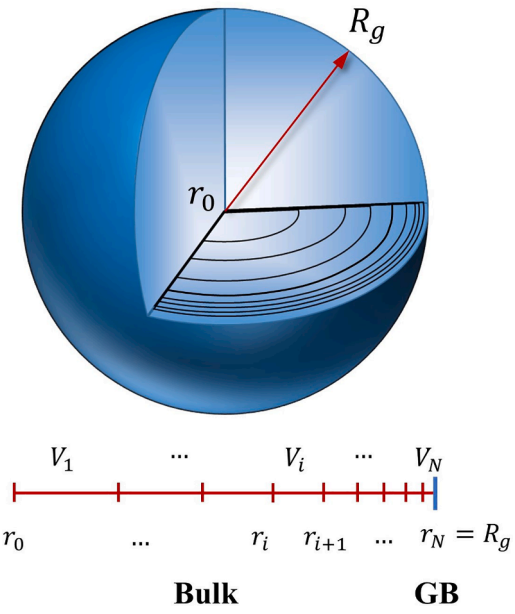

Fig. 1. Schematic illustration of the subdivision of a modelling spherical grain into spherical shells of geometric series. r_n and V_n represent the external radii and volumes of spherical shells.

$$x_v^{GB}(T) = x_v^{DJ}(T) = x_v^{eq}(T) \tag{1}$$

where $x_v^{GB}(T)$ and $x_v^{DJ}(T)$ are the vacancy site fractions at grain boundaries and at dislocation jogs respectively. $x_v^{eq}(T)$ represents the global equilibrium site fraction of vacancies.

In principle, the GB segregation process through diffusion of solute atoms to GB has also influence on the annihilation of excess vacancies at GBs. However, since the impurity diffusivity is several orders of magnitude lower than the vacancy diffusivity [35], this effect is rather limited. Thus, the solute concentration is assumed to be homogeneous across the grain in the following simulations.

2.1. Vacancy annihilation at grain boundaries

To simulate the vacancy annihilation at grain boundaries which relies on spatial diffusion of vacancy from grain center towards the GB, a finite volume method is used. As shown in Fig. 1, in the model, the modelling grain of spherical shape is divided into N concentric spherical shells with non-uniform external radii r_n ($n = 1, \ldots, N$) with $r_N = R_g$, where R_g is the radius of grain, as shown in Fig. 1. Moreover, the first shell becomes a sphere with a radius of r_1. Following the geometrical series, the shell thickness Δr_n is defined by

$$\Delta r_n = r_n - r_{n-1} = p \cdot q^{-n} = \frac{(1-q)q^N R_g}{1-q^N} \cdot q^{-n} \tag{2}$$

where p and q are two geometrical parameters. By generating the above non-uniform discrete series of shells, a more detailed distribution of vacancies in the vicinity of GB can be obtained without substantially increasing the computational cost.

Considering the mass conservation over each shell, free of hydrostatic stress, the temporal evolution of local site fraction of vacancies $x_v(n,t)$ is expressed as

$$V_n\left[\dot{x}_v(n,t) - \dot{s}_{jog}(n,t)\right] = A_{n-1}J_v^{n-1\to n}(t) - A_nJ_v^{n\to n+1}(t),\ n = 1, \cdots, N \tag{3}$$

where V_n and A_n are the volume and external area of the n-th shell, i.e.,

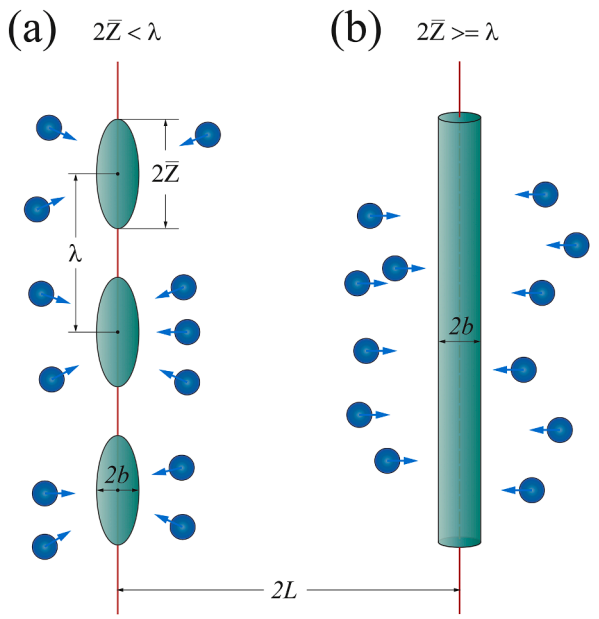

Fig. 2. Schematic illustrations of different modes of dislocation jogs as vacancy sinks in the cases (a) $2\overline{Z} < \lambda$ (jog mode) and (b) $2\overline{Z} \geq \lambda$ (line mode), where the blue arrows show vacancy fluxes. $\overline{Z}$ and λ represent the jog length and jog spacing, respectively, while L is the effective radius for collecting vacancies of the dislocation line.

$V_n = \frac{4}{3}\pi(r_n^3 - r_{n-1}^3)$ and $A_n = 4\pi r_n^2$. $\dot{x_v}(n,t)$ represents the change of $x_v(n,t)$, $\dot{s}_{jog}(n,t)$ the local annihilation rate of vacancies at dislocation jogs, which is described concretely in Section 2.2. $J_v^{n\to n+1}(t)$ represents the diffusive flux of vacancies from shell n to shell $n+1$, which is determined by the first Fick's law as

$$J_v^{n\to n+1}(t) = -D_v(T)\frac{dx_v(n,t)}{dr}\bigg|_{n\to n+1} \tag{4}$$

where $D_v(T)$ represents the diffusion coefficient of vacancies in the grain interior. In multi-component alloys, $D_v(T)$ needs to be corrected by the amounts of solute species and is defined as [20,23]

$$D_v(T) = \frac{D_{eff}}{f x_v^{eq}(T)},\quad D_{eff} = \sum_{i=0}^{k} x_i D_i^{eq}(T) \tag{5}$$

where f represents the geometrical correlation factor which has a value of 0.7815 for face-centered cubic crystals [35]. D_{eff} is the component-weighted diffusion coefficient, where x_0 and $D_0^{eq}(T)$ are the site fraction and self-diffusion coefficient of solvent, x_i and $D_i^{eq}(T)$ $(i \geq 1)$ the site fractions and impurity diffusion coefficients of solute atoms i, respectively. Conventionally, $D_i^{eq}(T)$ at a certain temperature $T(t)$ is given by

$$D_i^{eq}(T) = D_{i0}\exp\left(-\frac{\Delta Q_i^B}{k_B T}\right),\ i = 0, \ldots, k \tag{6}$$

where k_B is the Boltzmann constant, D_{i0} and ΔQ_i^B are the pre-factors and migration enthalpies for the diffusion of component i. Note that $x_v^{eq}(T)$ is also a function of alloy composition in multicomponent alloys and will be rigorously derived in Section 2.3.

The forward Euler scheme is applied to discretize $\dot{x_v}$ as

$$\dot{x_v}(n,t) = \frac{x_v(n,t) - x_v(n,t-\Delta t)}{\Delta t} \tag{7}$$

where the time interval Δt should be chosen as small as possible according to the trade-off between accuracy and efficiency. To accurately carry out the numerical simulations by using the present model, suitable initial condition and boundary conditions have to be chosen. The site fraction of vacancies across the grains is initialized to $x_v(n, t=0) = x_v^{eq}(T_{SS})$ after sufficient solution heat treatment at temperature T_{SS}. The von Neumann boundary condition is employed at the inner surface of the first spherical shell while the Dirichlet boundary condition is imposed for the last spherical shell, i.e.,

$$\begin{aligned} &J_v^{0\to 1}(t) = 0, \\ &x_v(N,t) = x_v^{GB}(T) \end{aligned} \tag{8}$$

More details of the numerical algorithm can be found in supplement S1.

In addition, the average site fraction of vacancies can be calculated by integrating the local site fraction in each shell over the whole bulk of the grain as

$$x_v^{avg}(t) = \frac{\sum_{n=1}^{N} V_n x_v(n,t)}{\sum_{n=1}^{N} V_n} \tag{9}$$

2.2. Vacancy annihilation at dislocation jogs

Based on the climb theory of edge dislocations proposed by Balluffi [31], the annihilation of excess vacancies at dislocation jogs is through two different modes. As shown in Fig. 2, the dislocation jogs positioning along dislocation lines with a spacing λ are normally considered as ellipsoidal sinks with semiaxes of $\overline{Z}$ and b and have a pseudo-spherically symmetric diffusion field around each of them when $2\overline{Z} < \lambda$. If the ellipsoidal sinks are overlapped with each other under the condition of $2\overline{Z} \geq \lambda$, the whole dislocation line become an ideal sink for excess vacancies and the surrounding diffusion field becomes cylindrical.

Given the quasi-steady state diffusion, the annihilation rate of vacancies at dislocation jogs in the jog mode, i.e., the vacancy flux entering the dislocation jogs, is defined by [31]

$$\dot{s}_{jog}(n,t) = -\frac{4\pi D_v H \overline{Z}\left[x_v(n,t) - x_v^{DJ}\right]}{\ln\left(\frac{2\overline{Z}}{b}\right)\left[1 + \frac{2\overline{Z}}{\lambda}\frac{\ln(L/\lambda)}{\ln(2\overline{Z}/b)}\right]},\ 2\overline{Z} < \lambda \tag{10}$$

where $x_v^{DJ}(T)$ is the vacancy site fraction on the surface of ellipsoidal sinks in equilibrium with the jog, herein set to be the equilibrium value $x_v^{eq}(T)$ in the grain interior at temperature $T(t)$. H represents the jog density, which, given the equilibrium jog spacing λ and the dislocation density ρ, can be calculated by $H = \rho/\lambda$. b is the Burgers vector of dislocation. L denotes the effective radius of each dislocation line where the vacancies are uniformly collected by and annihilated at the jogs distributed along the corresponding dislocation lines, which is associated with ρ as follows:

$$L = \frac{1}{\sqrt{\pi\rho}} \tag{11}$$

When $2\overline{Z} \geq \lambda$, the vacancy flux entering the dislocation line, i.e., the quasi-steady state annihilation rate of vacancies at dislocation jogs in the line mode is expressed as

$$\dot{s}_{jog}(n,t) = -\frac{2\pi D_v \rho\left[x_v(n,t) - x_v^{DJ}\right]}{\ln\left(\frac{L}{b}\right)},\ 2\overline{Z} \geq \lambda \tag{12}$$

More detailed derivations of $\dot{s}_{jog}(n,t)$ are included in supplement S2.

$\overline{Z}$ is determined by the mean migration distance of an attached vacancy on the dislocation line before jumping off as [31]

$$\overline{Z} = \sqrt{2}b\exp\left(\frac{\Delta Q_v^B - \Delta Q_v^D + \Delta E_{v-D}^B}{2k_B T}\right) \tag{13}$$

where ΔQ_v^B and ΔQ_v^D are the migration energy barriers of vacancy in the

bulk material and on the dislocation line, respectively. ΔE^B_{v-D} represents the binding energy of attached vacancy to the dislocation line. Moreover, the equilibrium spacing λ between jogs along the dislocation line under vacancy supersaturation is given by [32]

$$\lambda = b\exp\left(\frac{\Delta E^{F*}_{jp}}{2k_BT}\right) \tag{14}$$

where ΔE^{F*}_{jp} is the nucleation energy barrier of jog-pair on the dislocation line, which is derived as the maximum of jog-pair formation energy ΔE^F_{jp}. The formation of jog-pair is accompanied by the aggregation of attached vacancies on the dislocation line, therefore, ΔE^F_{jp} is expressed as [32]

$$\Delta E^F_{jp}(n_v) = E_{jp}(n_v) - n_v\cdot\Delta\mu_v \tag{15}$$

where $\Delta\mu_v$ represents the difference in chemical potential of vacancy far away from the jog versus at the jog and is given by $\Delta\mu_v(n,t) = k_BT\ln[x_v(n,t)/x_v^{DJ}]$ in the dilute limit. It is supposed that the jog-pair energy E_{jp} increases monotonically with the number of absorbed vacancies n_v [31,32]. According to the previous atomistic simulations [32,36], the jog-pair energy E_{jp} levels out to a value of $E^*_{jp} = 1.1$ eV beyond the critical number of absorbed vacancies, $n^*_v = 4$ for Al. Thus, once n^*_v vacancies have been absorbed between the jog pair, the jogs are regarded to be stable and become ideal sinks for additional vacancies.

Note that the dislocation density only shows a slight reduction during natural ageing and artificial ageing in the Al alloys [8], therefore, ρ is considered to be constant during heat treatments in the following simulations. In addition, as can be seen from the calculation in supplement S2, the vacancy depletion layer thickness around the dislocation jogs is only at the scale of nanometers, which is much smaller than the micron scale grain size. Therefore, a homogeneous vacancy concentration field is assumed for the same cell of bulk of grains.

2.3. Vacancy trapping by solute atoms and atom clusters

In multi-component alloys, the equilibrium vacancy site fraction is not only temperature-dependent but also composition-dependent, which is different from pure metals. Herein, the vacancy trapping is only considered at the first nearest neighbor (1NN) sites of solute atoms since the 1NN solute-vacancy interaction is significantly stronger than that at 2NN, 3NN and 4NN, for almost all the solutes in the Al matrix [37]. In addition, only solute atoms and atom clusters binding with one vacancy are considered since the probability of forming solute clusters binding with more vacancies is several orders of magnitude lower than the former type, as evaluated in Supplement S3, which is consistent with previous study [28]. In accordance with the thermodynamic analysis, the total number of vacancies can be classified into three groups [20]: trapped by individual solute atoms of component i having concentration x_i and Z neighboring sites ($Z = 12$ for fcc lattice), trapped by solute clusters containing N_{cl} atoms and having concentration x_{cl} and Z_{cl} closest neighboring sites, and those freely distributed in the matrix. Correspondingly, the equilibrium vacancy site fraction $x^{eq}_v(T)$ as a function of temperature and composition is expressed as follows [20,28]:

$$\begin{aligned} x^{eq}_v(T) &= \sum_{i=1}^{k} \underbrace{Zx_i\exp\left(-\frac{\Delta E^F_v}{k_BT}\right)\exp\left(\frac{\Delta E^B_{i-v}}{k_BT}\right)}_{x^{eq}_{i-v}} \\ &+ \sum_{cl} \underbrace{Z_{cl}x_{cl}\exp\left(-\frac{\Delta E^F_v}{k_BT}\right)\exp\left(\frac{\Delta E^B_{cl-v}}{k_BT}\right)}_{x^{eq}_{cl-v}} \\ &+ \underbrace{\left(1-(Z+1)\sum_{i=1}^{k}x_i - \sum_{cl}(Z_{cl}+N_{cl})x_{cl}\right)\exp\left(-\frac{\Delta E^F_v}{k_BT}\right)}_{x^{eq}_{v,rest}} \end{aligned} \tag{16}$$

Table 1
Thermodynamic and computational parameters in Al alloys used in the model.

Symbol	Meaning	Values	Units
D_{i0}	Diffusion pre-factors of Mg, Si, Cu, Zn and Al atoms	14.9, 13.8, 44.4, 11.9, 8.23 [41]	$mm^2\ s^{-1}$
ΔQ^B_i	Migration enthalpies of Mg, Si, Cu, Zn and Al atoms	1.249, 1.219, 1.388, 1.203, 1.276 [41]	eV
ΔQ^B_v	Migration enthalpy of vacancy in the bulk	0.55 [42]	eV
ΔQ^D_v	Migration enthalpy of vacancy in the dislocation core	0.45 [42]	eV
ΔE^B_{v-D}	Binding energy of attached vacancy to the dislocation core	0.181 [43]	eV
ΔE^F_v	Formation enthalpy of vacancy	0.67 [23]	eV
ΔE^B_{i-v}	Binding energies between Mg, Si, Cu, Zn, and Sn atoms and vacancies	0.01, 0.06, 0.03, 0.05, 0.24 [37]	eV
ΔE^B_{Mg-Si}	Binding energies between Mg and Si atoms	0.04 [37]	eV
ΔE^B_{MgSi-v}	Binding energies between Mg-Si pairs and vacancies	0.08 [44]	eV
b	Burgers vector for Al matrix	2.86	Å
k_B	Boltzmann constant	8.617×10^{-5}	$eV\cdot K^{-1}$

where ΔE^F_v represents the formation energy of individual vacancies in the Al matrix. ΔE^B_{i-v} and ΔE^B_{cl-v} represent the binding energies of individual vacancies to solute atoms of component i and to solute clusters cl in the Al matrix. The contribution of vibrational entropies is neglected since their impact on the prediction of vacancy site fraction is quite limited in comparation to other factors [34,38].

Provided that the relationship between the site fraction of vacancies trapped by component i, $x^{eq}_{i-v}(T)$, and that of total vacancies $x^{eq}_v(T)$ is not restricted to equilibrium, the non-equilibrium site fraction of trapped vacancies $x_{i-v}(n,t)$ can be derived from non-equilibrium vacancy site fraction $x_v(n,t)$ at every moment as

$$x_{i-v}(n,t) = \frac{x^{eq}_{i-v}}{x^{eq}_v}x_v(n,t),\ n = 1,\cdots,\ N \tag{17}$$

Herein, the trapped vacancies can be temporarily detached from the vacancy-solute atom complexes, meanwhile, new vacancies are bound to the individual solute atoms and/or solute clusters to maintain the local thermodynamic equilibrium condition until the global equilibrium state is reached [39,40]. The probability of the trapped vacancy escaping from the trapping site is controlled by the magnitude of binding energy between the vacancy and individual solute atoms and/or solute clusters, which can influence the average vacancy diffusivity according to Eq. (5).

3. Model evaluation

3.1. Influence of GB annihilation on evolution of excess vacancies

In the following simulation, the annihilation of excess vacancies in pure Al is considered as a benchmark case to evaluate the present numerical model in comparison to the FSAK model [23]. The polycrystalline Al is first solution heat treated at 873 K for a time sufficient to reach thermodynamic equilibrium, followed by quenching with a cooling rate of 100 $K\cdot s^{-1}$ to 423 K and then kept at this temperature. The radius of grain is set to be $R_g = 100$ μm and the dislocation-free grain is divided into $N = 400$ shells following the geometrical series with a factor of q=1.02. Other material data used in the model are listed in Table 1, which are also applied in the remaining simulations in this work.

Fig. 3 depicts the evolution of vacancies in pure Al during heat treatment in the presence of grain boundaries. The temperature history is illustrated in Fig. 3(a). As can be seen in Fig. 3(b), about 75% of the vacancies are lost due to GB annihilation during the quenching from 873K to 423 K. However, the average site fraction of vacancies after

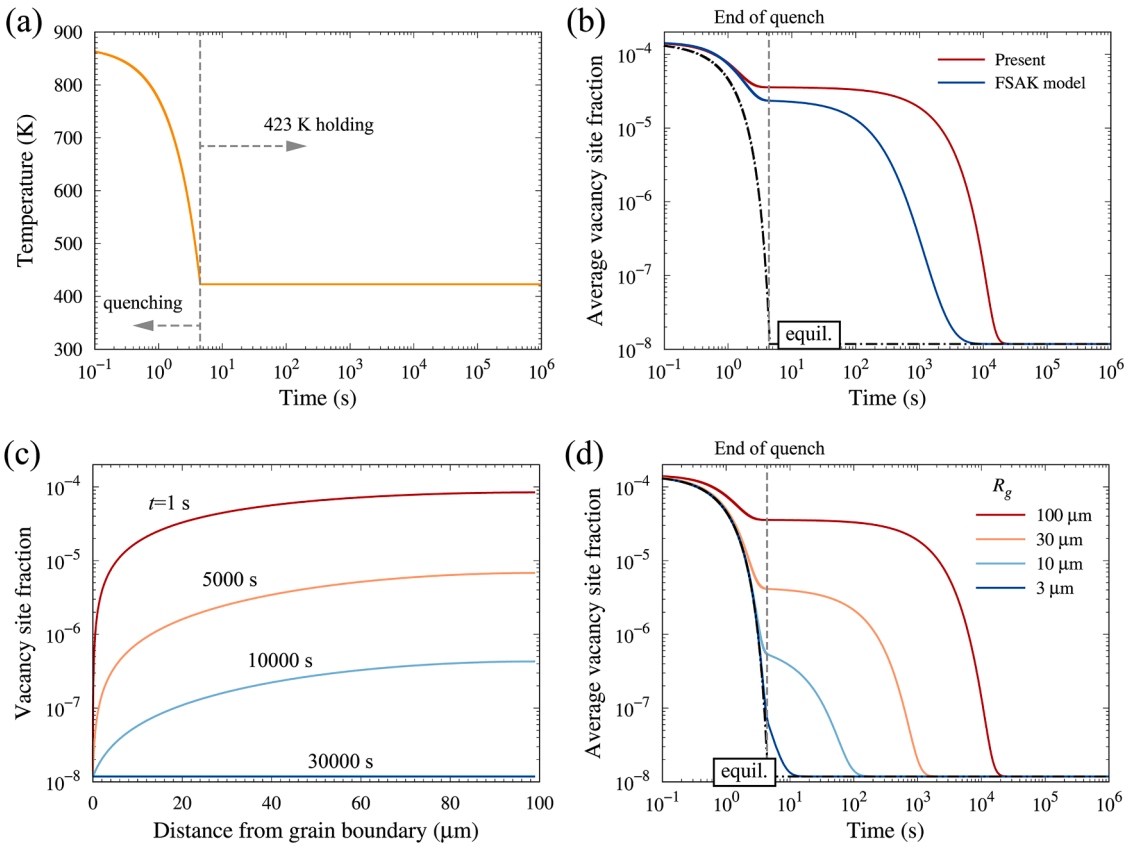

Fig. 3. Calculated time evolution of vacancies in pure Al during quenching from 873 K with 100 K · s^{-1} cooling rate and holding at 423 K in the presence of grain boundaries. (a) The change of temperature with time; (b) Comparison of the evolution of average vacancy site fraction between the present model and the FSAK model [23] under the condition of $R_g = 100$ μm; (c) Evolution of spatial distribution of vacancies across the grain with holding time; (d) Time evolutions of average vacancy site fraction for various grain sizes. The dot-dash lines in (b) (d) represent the equilibrium vacancy site fraction corresponding to the temperature history.

quenching is still more than three orders of magnitude higher than the equilibrium counterpart at the temperature (dot-dash line). In this work, the equilibrium vacancy site fraction corresponding to the temperature history is always represented by dot-dash lines. During isothermal heat treatment at 423 K, the vacancy site fraction gradually decreases with increasing time due to the annihilation of vacancies at GB, and it takes about 2×10^4 s until it reaches the equilibrium value at the temperature. In contrast, it takes about 5×10^3 s for the vacancies to reach the equilibrium site fraction when using the FSAK model and only considering GB annihilation [23], demonstrating that the present model predicts a significantly lower annihilation rate of vacancies at GB. The difference in predicted annihilation kinetics of vacancies is attributed to the assumption of the homogeneous distribution of vacancies over the whole grain in the FSAK model, which results in an overestimation of the vacancy annihilation rate. Fig. 3(c) illustrates the evolution of spatial distribution of vacancies across the grain with holding time. It can be clearly seen that the vacancy site fraction at GBs reaches the equilibrium value instantaneously, thus creating a concentration gradient of vacancy from the bulk to the GBs. With holding time increasing, all the excess vacancies are gradually annihilated at the GB sink and the vacancy site fraction eventually decays to the equilibrium value in the whole bulk grain. Fig. 3(d) shows the evolutions of average vacancy site fraction in pure Al for various grain radii. As can be seen, the annihilation rate of vacancies increases with reducing grain size. For a grain of $R_g = 3$ μm, after quenching to 423 K the vacancy site fraction has already reduced to 6×10^{-8}, and it takes only 6 s for the vacancy site fraction to reach the equilibrium value, indicating that excess vacancies are difficult to preserve after quenching in small grains.

3.2. *Influence of dislocation jogs on annihilation of excess vacancies*

A single crystal of pure Al without GBs is chosen to evaluate the influence of dislocation jogs on the annihilation of excess vacancies. The thermal heat treatment condition is the same as that used in Section 3.1. The dislocation lines are assumed to be uniformly distributed in the grain and a typical dislocation density value of well-annealed aluminium alloys $\rho = 10^{11}$ m^{-2} [23,45] is selected.

Fig. 4 displays the time evolution of vacancies and the corresponding evolutions of jog spacing and jog length during quenching and the subsequent isothermal heat treatment of pure Al in the presence of dislocations. As shown in Fig. 4(a), although the annihilation of vacancies at GBs is neglected, the reduction of vacancy site fraction during the cooling process of quenching is even faster than that of grains of 100 μm in size (Fig. 3(b)), indicating that dislocation jogs play an important role in the vacancy annihilation during quenching even for the fully annealed alloy. Moreover, the present model shows slower vacancy annihilation kinetics during both quenching process and holding process than the FASK model when only considering vacancy annihilation at dislocation jogs. This is due to the different assumptions on dislocation jog distribution in the two models, where the FASK model assumed homogeneously distributed individual jogs of fixed spacing of $50b \approx 7 \times 10^{-8}$ m as spherical sinks for vacancies during the whole heat treatment [23]. As illustrated in Fig. 4(b), our model shows the spacing of dislocation jogs and the corresponding vacancy annihilation modes at dislocation jogs indeed change with temperature and holding time. During the cooling process of quenching, the jog spacing λ decreases with decreasing temperature but remains larger than the jog length $2\bar{Z}$, so the jogs act as ellipsoidal sinks for vacancies at this stage. Meanwhile,

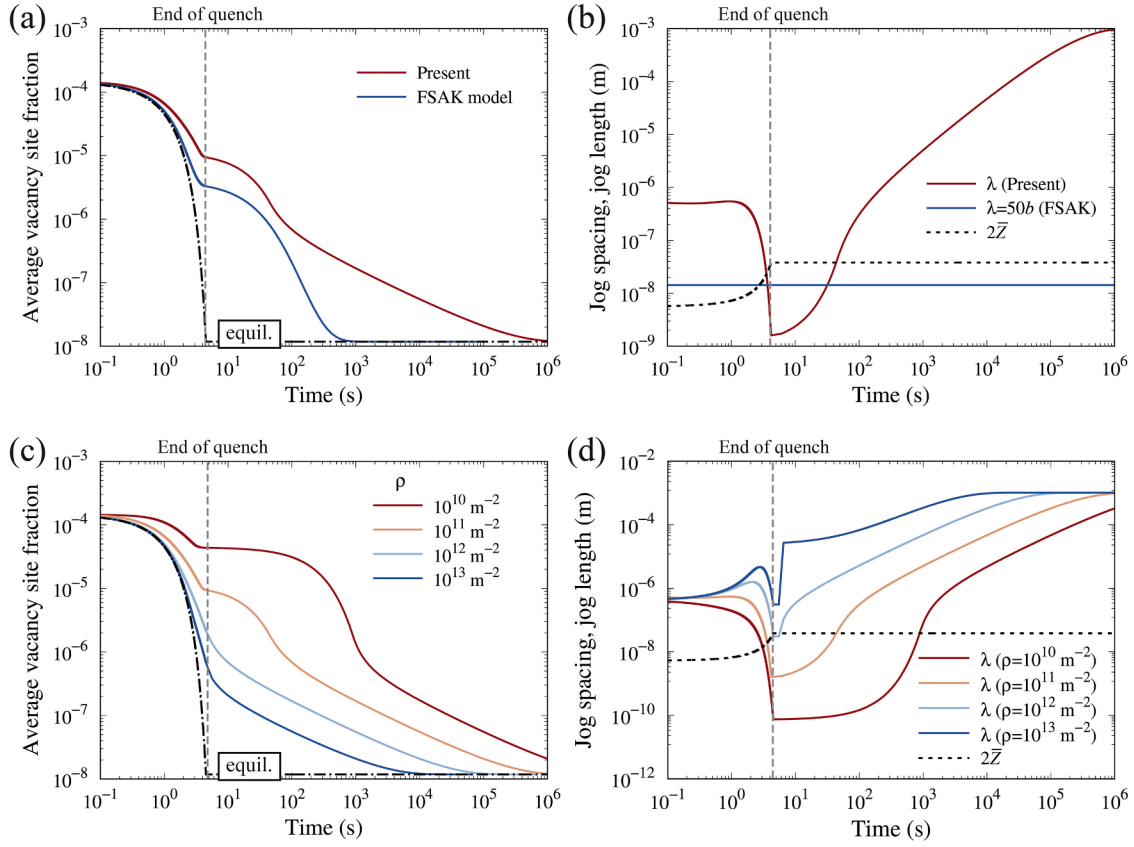

Fig. 4. Calculated time evolution of vacancies in pure Al during quenching from 873 K with 100 $K \cdot s^{-1}$ cooling rate and holding at 423 K in the presence of dislocations. (a) Comparison of the evolution of vacancy site fraction between the present model and the FSAK model [23] under the condition of $\rho = 10^{11}$ m^{-2}; (b) Evolutions of spacing and length of dislocation jogs; Influences of dislocation density on the evolution of (c) vacancy site fraction and (d) jog spacing λ.

the jog length $2\overline{Z}$ monotonically increases to a value larger than λ at the end of quenching. During isothermal heat treatment, the jog spacing shows a monotonic increase with increasing holding time while the jog length remains constant. Within around 50 s after quenching, the condition $2\overline{Z} > \lambda$ is satisfied. Therefore, the entire dislocation core becomes a perfect line sink for vacancies and the vacancy annihilation kinetics becomes faster during this period as shown in Fig. 4(a). Afterwards, the jog spacing exceeds the jog length so that the jogs change to be ellipsoidal sinks again. In the meantime, the annihilation rate of vacancies becomes slower due to the continuous decrease of jog density. Fig. 4(c) and (d) further demonstrates the influence of dislocation density on the time evolution of vacancies in pure Al. It can be found in Fig. 4(c) that annihilation rate of vacancies increases with increasing dislocation densities. Furthermore, when ρ is larger than a certain value (around 10^{12} m^{-2}), the jogs can only act as ellipsoidal sinks for vacancies because the annihilation rate is so fast that the vacancy supersaturation is not sufficient to form perfect line sinks, as shown in Fig. 4(d).

Moreover, the effect of the transition between the two vacancy annihilation modes at dislocation jogs on the vacancy annihilation rate is further evaluated. As shown in Fig. S2 in the supplement, only considering the line mode where a continuous cylindrical diffusion field around dislocations lines is used will pronouncedly overestimate the

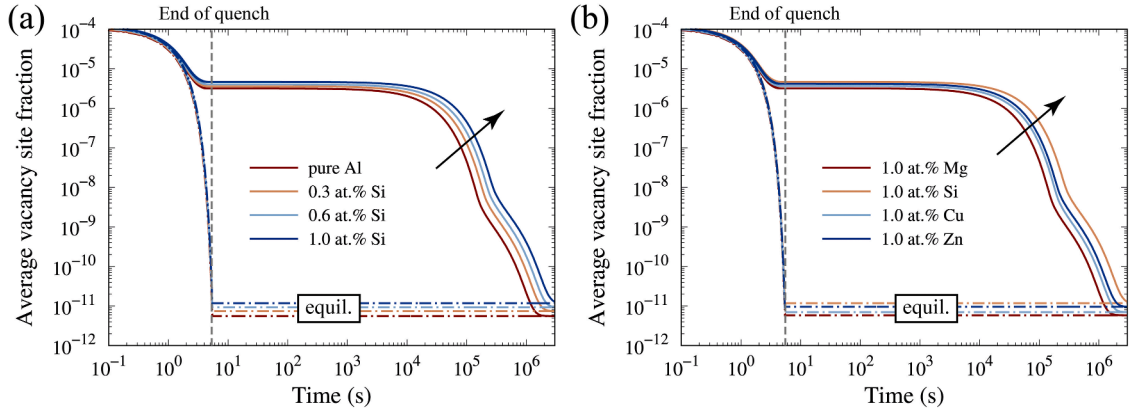

Fig. 5. Calculated time evolution of vacancies in various binary Al alloys during quenching from 873 K with 100 $K \cdot s^{-1}$ cooling rate and ageing at 298 K in the presence of dislocation jogs ($\rho = 10^{11}$ m^{-2}) and grain boundaries ($R_g = 30$ μm). (a) Al-Si binary alloy with different Si contents; (b) Different Al-X alloys containing 1 at. % solute element X (X=Mg, Si, Cu, Zn).

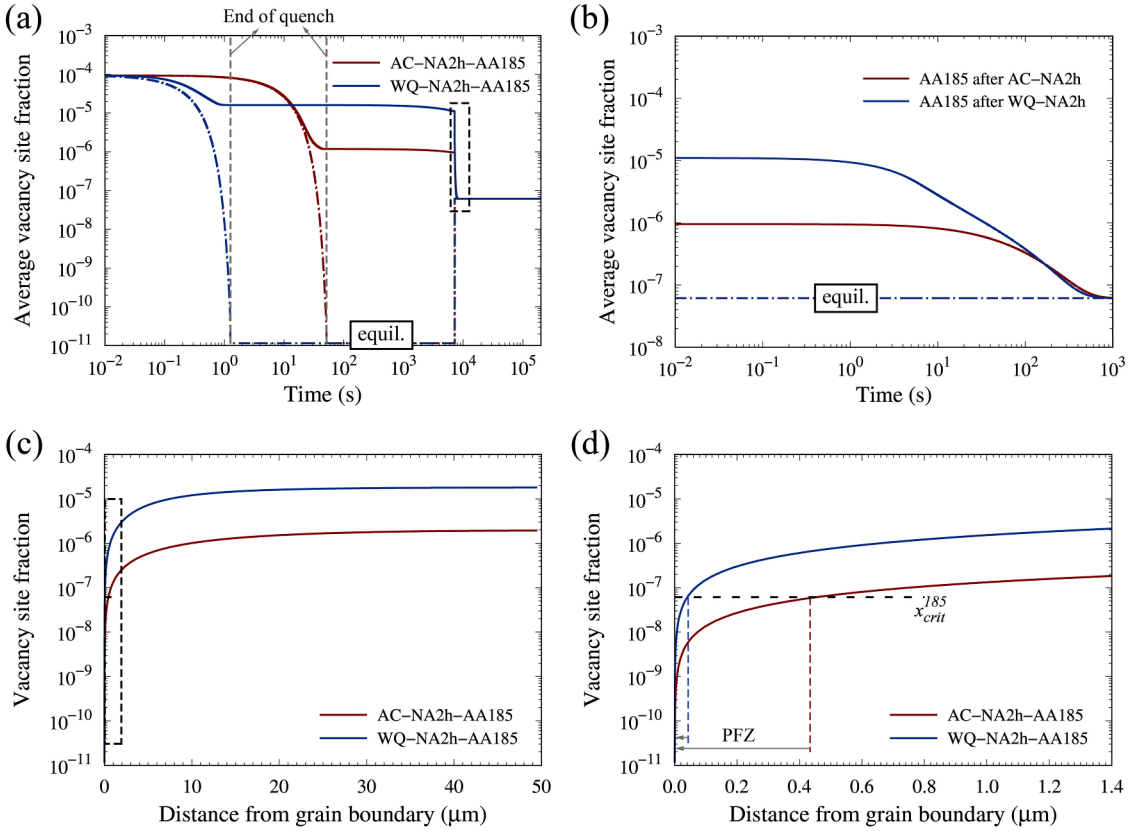

Fig. 6. Calculated time evolution of vacancies in an Al-Mg-Si(-Cu) alloy during cooling from 550 ℃, storage at RT for 2h, and subsequently ageing at 185 ℃. (a) Comparison of the evolution of average vacancy site fraction under the conditions of AC and WQ; (b) The enlarged figure of framed area in (a), where the time indicates the AA time; (c) Spatial distribution of vacancies across the grain at the beginning of AA; (d) The enlarged figure of framed area in (c).

vacancy annihilation rate in comparison to the model considering the mode transition. In contrast, there is only a small difference in vacancy site fraction when assuming vacancy annihilation only in the jog mode, i.e., the number of excess vacancies retained after quenching from solution temperature and during isothermal holding are not remarkably changed. Therefore, a simplification of the model by assuming only jog mode will not significantly influence the final vacancy annihilation rate. However, for the sake of integrity and rationality, it is better to include the vacancy annihilation mode transition in the model [31,46,47].

3.3. Influence of solute trapping on the evolution of excess vacancies

Mg, Si, Cu and Zn are the major alloying elements in age hardening Al alloys, i.e., 2xxx, 6xxx and 7xxx alloys. In this section, the trapping of vacancies by solute atoms in different binary aluminium alloys has been examined. The thermal history of the binary alloys involves quenching from 843 K at 100 $K \cdot s^{-1}$, followed by natural ageing at 298 K. The radius of grain and dislocation density are set as $R_g = 30$ μm and $\rho = 10^{11}$ m^{-2}, respectively.

Fig. 5 demonstrates the time evolution of vacancy site fraction in various binary Al alloys under ageing heat treatment in the presence of both GBs and dislocations. As can be seen in Fig. 5(a), the equilibrium vacancy site fraction increases with increasing Si contents, which is more significant at lower temperatures. Meanwhile, the vacancy annihilation kinetics is slower at higher Si contents. As shown in Fig. 5(b), with 1 at.% content of different solutes, the equilibrium vacancy site fraction at room temperature (RT) is the largest in Al-Si (ΔE^B_{Si-v}= 0.06 eV) alloy, followed by Al-Zn (ΔE^B_{Zn-v}=0.05 eV), Al-Cu (ΔE^B_{Cu-v}=0.03 eV) and finally the Al-Mg (ΔE^B_{Mg-v}=0.01 eV) alloy [37]. The vacancy annihilation kinetics follows the same trend. It implies that solute elements with stronger binding to vacancies are more capable of binding with excess vacancies and retarding their annihilation in Al alloys.

4. Application of model

4.1. Influences of heat treatment on PFZ formation in 6xxx alloys

It is known that the vacancy distribution across grains plays an important role in the formation of precipitate-free zones (PFZ) near GBs during artificial ageing. In this section, the evolution of vacancies in an experimental 6005A alloy (Mg 0.63, Si 0.62, Cu 0.06, Fe 0.10, Mn 0.08, all in at.%) has been simulated, by using the same artificial ageing treatment parameters as used by Marioara et al. [48]. In this work, the authors studied the PFZ evolution in the alloy under three different heat treatments, AC-NA2h-AA185, WQ-NA2h-AA185 and WQ-NA2h-AA210, in which the letters and numbers indicate the cooling method from solution treatment at 550 ℃ (WQ: water quenching at 400 $K \cdot s^{-1}$, AC: air cooling at 10 $K \cdot s^{-1}$), natural ageing (NA) time (2h) and artificial ageing (AA) temperatures (185 and 210 °C). The grain radius and dislocation density are set to be $R_g = 50$ μm and $\rho = 10^{11}$ m^{-2}, respectively. In the following simulations, the presence of Fe and Mn is neglected since they have little influence on the trapping of vacancies. Among different atom clusters, only Mg-Si pairs in the first nearest neighbor inherited from the solid solution treatment at temperature T_{SS}, are regarded as trapping sites for vacancies, while the other clusters are neglected since their site fractions are several orders of magnitude lower than that of individual solute atoms. In thermodynamic equilibrium at T_{SS}, the concentration of Mg-Si pairs can be calculated by [28,49]

$$x_{MgSi} = Z x_{Mg} x_{Si} \exp\left(\frac{\Delta E^B_{Mg-Si}}{k_B T_{SS}}\right) \tag{18}$$

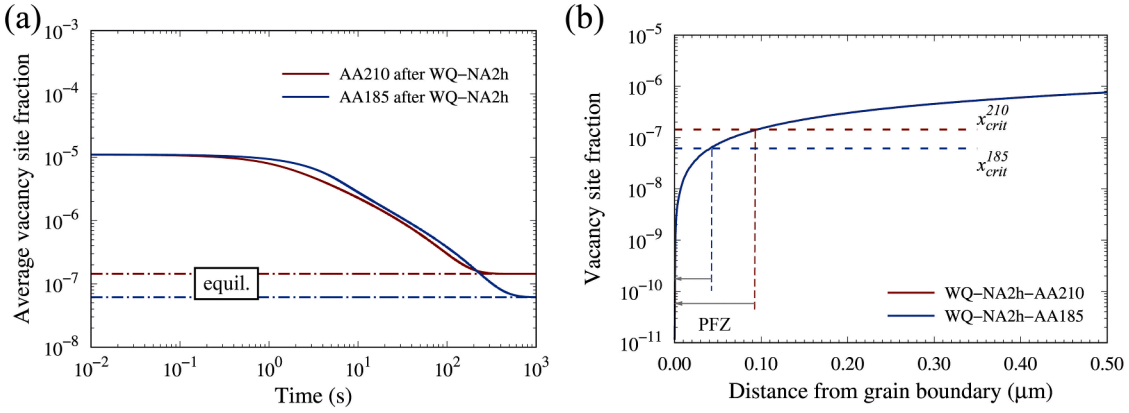

Fig. 7. Calculated time evolution of vacancies in an Al-Mg-Si(-Cu) alloy during AA after WQ from 550 ℃ and storage at RT for 2h. (a) Comparison of the evolution of vacancy site fraction under the conditions of AA at 210 ℃ and 185 ℃; (b) Spatial distribution of vacancy site fraction in the vicinity of GB at the beginning of AA under the corresponding conditions, the assumed critical vacancy site fractions at 185 and 210 ℃ are shown as dashed lines.

where ΔE^{B}_{Mg-Si} is the binding energy between Mg and Si atoms in the Al matrix. Moreover, the cluster-related parameters for Mg-Si pairs are assumed to be Z_{Mg-Si}=12 and N_{Mg-Si}=2, which are the same as the approximations in [20].

Fig. 6(a) shows the influence of cooling methods (AC and WQ) on the evolution of vacancy site fraction in the Al-Mg-Si-Cu alloy during quenching, NA and AA processes. As can be seen, the site fraction of vacancies after cooling by WQ is about 15 times as that of AC. This is because the excess vacancies have more time to diffuse to and be annihilated at different sinks during quenching by AC. During NA, the vacancy site fraction decreases slowly with increasing time. After 2h NA, about 81% and 68% of the quenched-in vacancies are retained for AC and WQ conditions, respectively. However, during AA, the vacancy site fraction decreases quickly, reaching the equilibrium value within 10^3 s, which is due to the high diffusivity of vacancies at 185 °C, as shown in Fig. 6(b). To further reveal the influence of quenching method on the annihilation of vacancies, spatial distribution of vacancies across the grain at the beginning of AA is plotted in Fig. 6(c), while the region close to the grain boundary is shown in Fig.6(d). The total vacancy site fraction in the WQ alloy is ~10 times higher than that of AC. In the experimental work [48], the average widths of PFZ were determined as ~200 nm and ~61 nm after AA for 2 hours for AC and WQ conditions, respectively, showing a difference of approximately 4 times. Since the

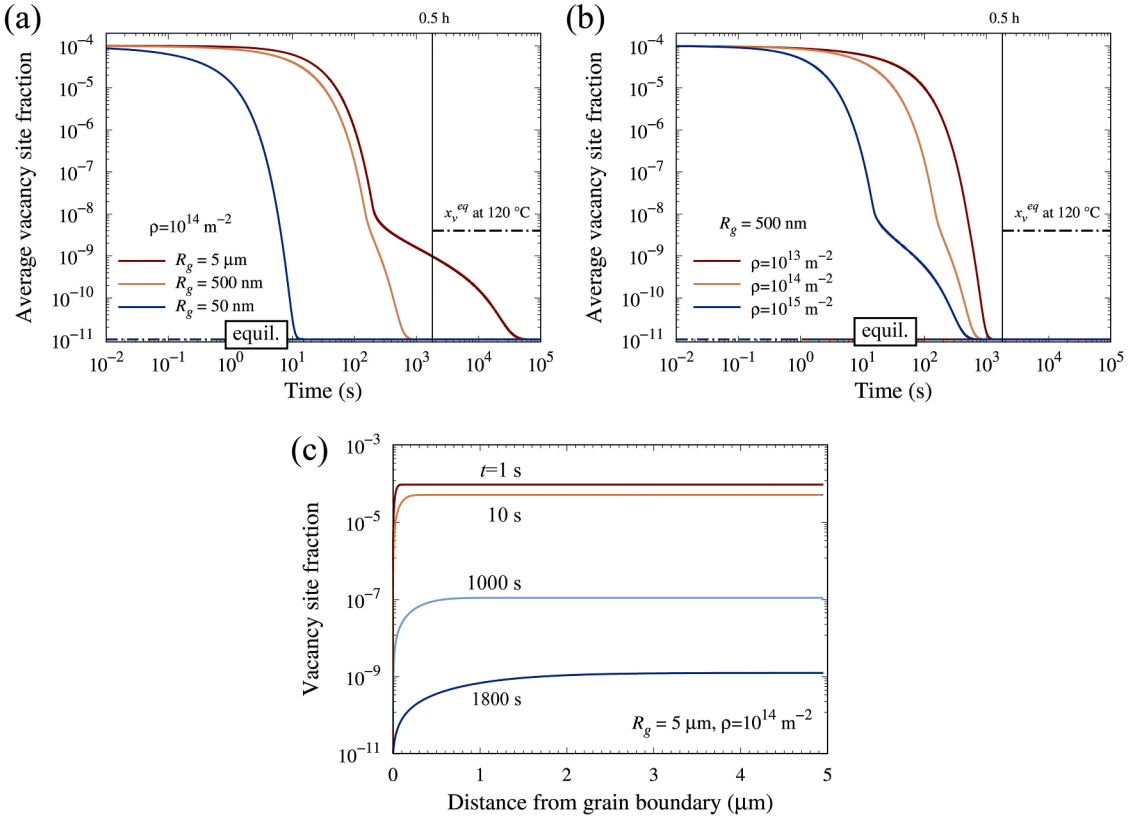

Fig. 8. Calculated time evolution of vacancies in an Al-5Cu alloy after 5 passes of ECAP during post-ECAP NA treatment. Comparison of the evolution of vacancy site fraction (a) for various grain sizes and (b) for various dislocation densities; (c) Evolution of spatial distribution of vacancies across the grain in the case of $\boldsymbol{R_g}$ = 5 μm and $\boldsymbol{\rho}$ = 10^{14} m^{-2}.

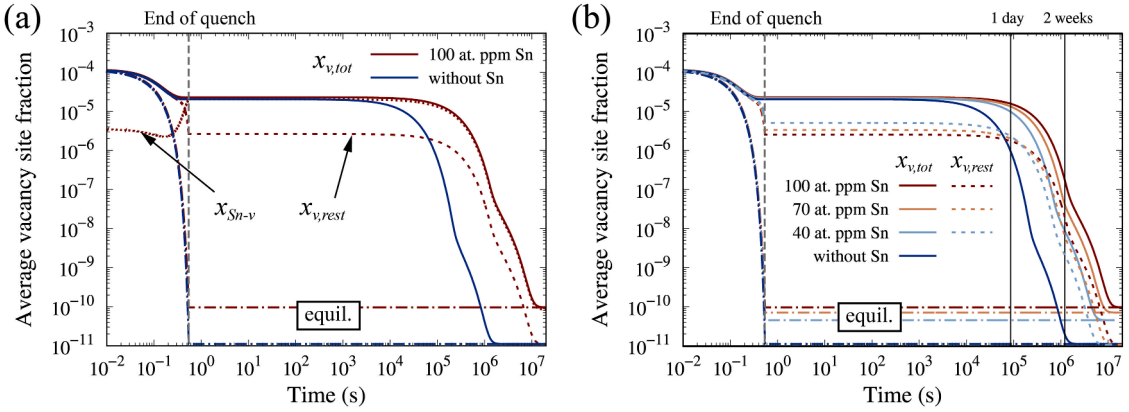

Fig. 9. Calculated time evolution of vacancies in an Al-Mg-Si(-Sn) alloy with and without Sn addition during quenching from 843 K at 1000 K · $s^{-1}$and storage at RT. (a) In the case of 100 at. ppm Sn addition; (b) Comparison of the evolution of vacancies under different amounts of Sn addition.

depletion of vacancy in the vicinity of GBs is considered as an important cause for the formation of PFZs, there may exist critical values of vacancy site fraction, x_{crit}^{T}, necessary for the age hardening precipitates to form at AA temperature of T [12,13]. In the present simulation, by assuming $x_{crit}^{185} = x_v^{eq}(185°C)$, the PFZ width could be determined in Fig. 6(d), and it can be seen that the PFZ width under AC condition is about 10 times larger than that under WQ condition, which is in reasonable agreement with the experimental results and qualitatively interprets the significant influence of the quenching mode on the PFZ width.

Fig. 7 (a) shows the influence of AA temperature on the time evolution of excess vacancies during AA after WQ and NA for 2 h. As can be seen, the equilibrium site fraction of vacancies is higher at 210 °C, which also shows a faster annihilation kinetics than AA at 185 °C. The average widths of PFZs were experimentally measured as ~66 nm and ~61 nm after AA for 2 hours for AA210 and AA185 conditions, respectively [48]. Embury et al. [12] suggested that x_{crit}^{T} was bigger at higher AA temperatures because at a lower solute supersaturation, a higher number of vacancies was required for nucleation of precipitates. Therefore, a bigger x_{crit}^{T} is selected at a higher AA temperature of 210 C, i.e., $x_{crit}^{210} = x_v^{eq}(210°C)$. As illustrated in Fig. 7(b), although the vacancy distribution close to the GB almost overlaps with each other, the corresponding PFZ width is predicted to be 2 times larger under WQ-NA2h-AA210 condition, which qualitatively interprets the influence of AA ageing temperature on the PFZ width as observed in the experimental work. The absolute values of x_{crit}^{185} and x_{crit}^{210} suggested here are only used to qualitatively assess the relative sizes of PFZs under different conditions.

It has to be noted that the main objective of this model is not to quantitatively predict the formation of PFZ, but to qualitatively explain the influence of excess vacancies on PFZ width. In addition to the rapid annihilation of vacancies at GBs, the depletion of solutes in the vicinity of GBs due to segregation of solutes to GBs, formation of GB precipitates and coarsening of age hardening precipitates also contribute to the evolution of PFZ width in age hardening Al alloys [6,13,50,51]. The difference in PFZ width between the simulation results shown in Fig. 6 (d) and Fig. 7(b) and the experimental results in [48] can be attributed to the neglection of latter factors in the present model, which are expected to appear within 2h of AA. The simplification of the temperature change during quenching can also cause the difference, which is more complicated in practice. Despite the difference in the exact value of PFZ width, the dependencies of the formation of PFZ along GBs during the early stage of AA on cooling rate during quenching, NA, and temperature of AA can be well explained.

4.2. *Influence of severe plastic deformation on the precipitation in Al-Cu alloy*

It has long been known that the precipitation behavior of age hardening precipitates in aluminium alloys processed by severe plastic deformation (SPD) is largely different from that after normal solution treatments. Instead of forming nano-sized coherent or semi-coherent metastable precipitates in bulk of grains, precipitation of coarse stable precipitates occurs along GBs even during NA [8,52]. In the experimental work [8], an Al-5Cu (wt.%) alloy processed by equal channel angular pressing (ECAP) was stored at RT for 30 minutes, and then artificially aged at 120 °C. Herein, the time evolution of vacancies in this nanostructured Al-5Cu alloy during NA is simulated. Since the major objective is not to reproduce the whole evolution of vacancies during ECAP, the simulation is set to start immediately after deformation. The grain size and dislocation density of the as-deformed Al-5Cu alloys have been taken according to the experimental measurement in [7]. Different grain size of $R_g = 50$ nm, 500 nm and 5 μm have been assessed, while the dislocation density is set as $\rho = 10^{14}$ m^{-2}. The initial site fraction of vacancies after SPD is assumed to be 10^{-4} as estimated in [53]. The formation of Cu clusters and precipitates is not considered in this simulation.

Fig. 8 illustrates the time evolution of vacancies in the as-deformed Al-5Cu alloy during post-ECAP NA treatment. As shown in Fig. 8(a), it takes approximately 10 s and 800 s for the vacancy site fraction to reach the equilibrium value, for grains of $R_g = 50$ nm and 500 nm, respectively. It indicates that the excess vacancies are annihilated rapidly in the nano- or ultrafine-grained SPD alloys during NA. In the relatively coarse micron-sized grains of $R_g = 5$ μm, although it takes longer time, 10^4 s, for the vacancies to reach the equilibrium site fraction, the vacancy site fraction after 0.5h RT storage has decreased down to a value lower than the equilibrium site fraction at 120 °C. The influence of dislocation density on the vacancy evolution is further illustrated in Fig. 8(b). As can be seen, the annihilation kinetics of excess vacancies is faster in grains of higher dislocation density. However, with a relatively lower dislocation density, 10^{13} m^{-2}, the vacancy site fraction decays to the equilibrium value within 10^3 s. Therefore, the rapid vacancy annihilation kinetics in the as-deformed Al-5Cu alloy is attributed to both ultrafine grain sizes and high dislocation densities, which gives rise to the lack of excess vacancies during NA and subsequent AA, thus resulting in the suppression of homogeneous nucleation of coherent or semi-coherent metastable precipitates in bulk of grains. Although the preferentially heterogeneous nucleation of coarse stable precipitates along the dislocations also plays an important role, the simulated results by the present vacancy annihilation model can qualitatively interpret the abnormal precipitation behavior observed in SPD-processed materials [8,52].

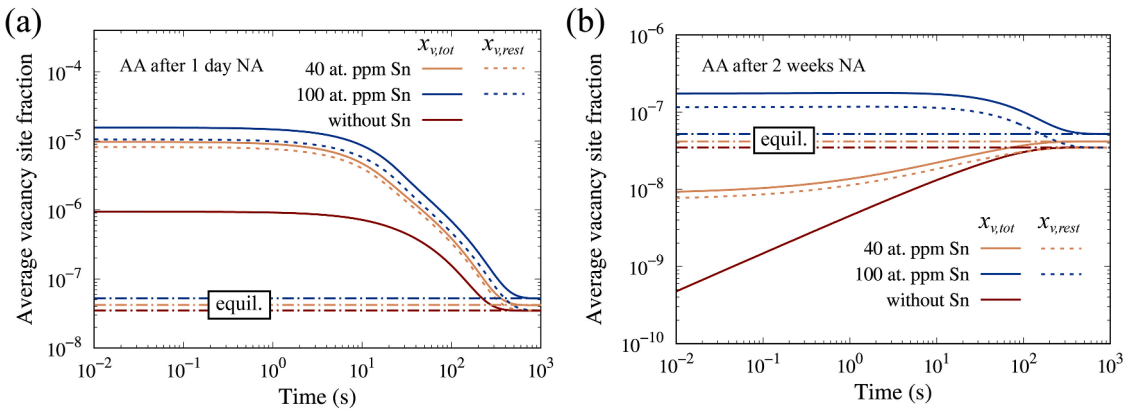

Fig. 10. Calculated time evolution of vacancies in an Al-Mg-Si(-Sn) alloy with and without Sn addition during artificial ageing at 443 K after (a) 1 day and (b) 2 weeks of RT storage.

As shown in Fig. 8(c), the number of excess vacancies across the whole grain after 0.5h RT storage has decreased to a remarkably low level, thus producing a PFZ of a width comparable to grain size during subsequent AA. Similar observations can also be found in the nano-scale APT samples [54], where the suppressed clustering kinetics at a lower temperature after quenching from solution heat treatment is attributed to rapid annihilation of non-equilibrium excess vacancies at the free surface of the nano-scale object.

4.3. Influence of impurity Sn atoms on the precipitation behavior of 6xxx alloys

Sn has been reported to be an effective alloying element to retard the deleterious effect of NA on the subsequent AA in 6xxx Al alloys, which has been attributed to its strong binding to vacancies [29]. In the experimental work [29], no clustering of Mg and Si could be observed by atom probe tomography in the 6061 alloy with an addition of 100 at. ppm Sn during 2 weeks of RT storage after quenching. It has also been suggested that the diffusivity of Sn-vacancy complexes is several orders of magnitude lower than that of free vacancies [28], which implies that the excess vacancies bound to Sn have little contribution to the diffusion of Mg and Si atoms. Thus, it is necessary to track the evolution of the number of vacancies which are trapped and not trapped by Sn separately, i.e., x_{Sn-v} and $x_{v,rest} = x_{v,tot} - x_{Sn-v}$. Following [25], solution treatment temperature of 843 K, cooling rate of water quenching (1000 $K \cdot s^{-1}$) to room temperature (300 K) and AA temperature of 443 K are applied in the simulation. The nominal composition is set to be Al-0.90 Mg-0.59 Si (in at. %) with trace amounts of Sn. The grain radius and dislocation density are chosen as $R_g = 25$ μm and $\rho = 10^{11}$ m^{-2}, respectively. Similarly, only individual solute atoms and Mg-Si co-clusters are treated as trapping sites for vacancies in this simulation.

Fig. 9(a) illustrates the time evolution of vacancies in the alloys without and with 100 at. ppm Sn addition during quenching and NA at RT. As can be seen, with Sn addition, the equilibrium vacancy site fraction at RT is increased by one order of magnitude due to the trapping of vacancies by Sn atoms; meanwhile, the annihilation rate of vacancies is significantly reduced by a factor of around 10. However, in the Sn-containing alloy $x_{v,rest}$ is approximately one order of magnitude lower than in the Sn-free counterpart after quenching and last until 10^4 s NA. With such a low concentration of free vacancies, it can be expected that the formation and growth of atom clusters during NA is remarkably retarded. As depicted in Fig. 9(b), as the amount of Sn increases, the site fraction of free vacancies $x_{v,rest}$ is decreasing, showing that the retardation effect of Sn on the clustering kinetics during NA increases with the solute Sn content in the alloys. Moreover, it takes longer time for both $x_{v,rest}$ and $x_{v,tot}$ to reduce to the equilibrium levels.

Fig. 10 shows the time evolution of vacancies in the alloys with and without Sn addition during AA at 443 K, after storage at RT for both 1 day and 2 weeks as labelled in Fig. 9(b). As illustrated in Fig. 10(a), vacancies are quickly annihilated at different sinks within only 10^3 s during AA due to the higher diffusivity of vacancies at higher temperatures. Nevertheless, after NA for 1 day, the total site fraction of vacancies in the Sn-containing alloys is one order of magnitude higher than that in the Sn-free alloy. Since the trapping of vacancies by Sn atoms is relatively weaker at higher temperatures, the vacancies trapped by Sn during NA are released during AA, and the site fraction of free vacancies $x_{v,rest}$ in the Sn-containing alloys is about 10 times higher than the Sn-free alloy. Moreover, $x_{v,rest}$ increases with increasing Sn content, which implies a faster precipitation kinetics during AA. As can be seen in Fig. 10(b), after 2 weeks NA, both $x_{v,rest}$ and $x_{v,tot}$ in the alloy with 100 at. ppm Sn is much higher than the equilibrium vacancy site fraction at AA temperature of 443 K. In contrast, the site fractions of free vacancies in the alloy with 40 at. ppm Sn addition and in the Sn-free alloy are lower than the equilibrium value at the beginning of AA. Hence, it can be expected that the precipitation kinetics in the two alloys during AA will be reduced by the long time NA. This modelling result is in good agreement with the experimental results by Pogatscher et al. [29].

5. Discussion

Over the last decades, plenty of models have been developed to simulate the age hardening precipitation kinetics in Al alloys during heat treatments [10,55-61]. In most of the models, the influences of excess vacancies on precipitation kinetics are not taken into account. Therefore, it is difficult to predict the influences of cooling rate during quenching, room temperature storage after solution treatment, dislocation structure, and grain size on the age hardening behavior during AA. The simulation results on the spatial evolution of vacancies during heat treatment in the present work have demonstrated the important roles of excess vacancies in the precipitation of age hardening precipitates in the widely used heat treatable Al alloys. In addition to the successful application examples on PFZ formation, abnormal precipitation behaviors of UFG Al-Cu alloys processed by ECAP, and the retarding effect of Sn on the annihilation of vacancies during NA, the present vacancy evolution model will also help to better understand the age hardening kinetics of heat treatable Al alloys. On one hand, the presence of sufficient excess vacancies is crucial for the formation of high density ordered solute atom clusters or GP zones in 6xxx alloys, which later develop into age hardening precipitates. Previous studies have shown that vacancy is important for the formation of "eye" like unit cells of β'' precipitates, where each "eye" needs one vacancy to facilitate the shift of central Mg atoms into the interstitial positions of FCC Al unit cells [62,63]. Such a shift reduces the misfit strain between the precipitates and surrounding Al matrix and therefore the formation energy [12,37]. On

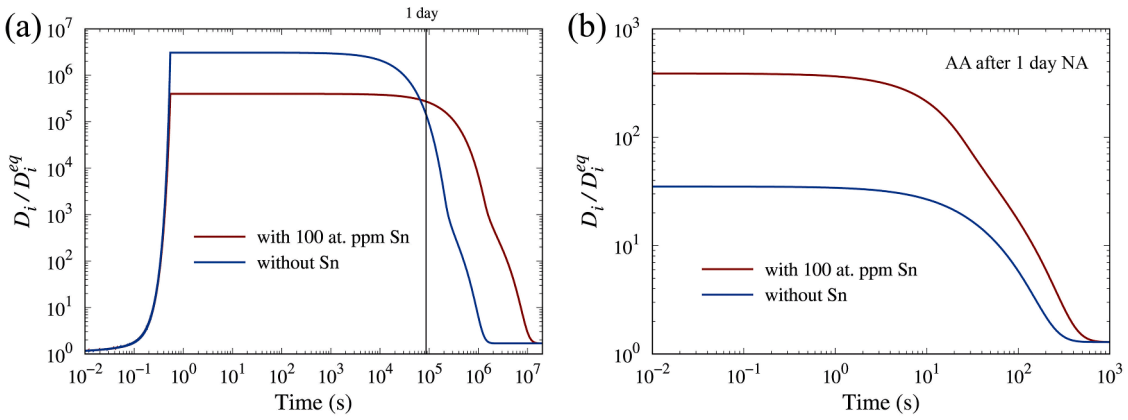

Fig. 11. Enhancement factor of solute diffusivity (i = Mg, Si) by excess vacancies in an Al-0.90 Mg-0.59 Si (in at. %) with and without Sn addition (a) during quenching from 843 K at 1000 K · s^{-1} and storage at RT (300 K), and (b) during artificial ageing at 443 K after 1 day of RT storage.

the other hand, excess vacancies can enhance the diffusivities of substitutional solute atoms, accelerating the precipitation kinetics. The intrinsic diffusion coefficients of substitutional solute atoms can be written as [35,64]

$$D_i(T) = f_2^i \Gamma_2^i a^2 x_v \exp\left(\frac{\Delta E_{i-v}^B}{k_B T}\right) \tag{19}$$

where f_2^i and Γ_2^i represent the correlation factor and transition frequency of the solute atoms of component i in the dilute limit, a is the lattice constant. For each component i, D_i is proportional to the vacancy site fraction. Therefore, the solute diffusivity in the presence of excess vacancy can be enhanced by a factor of

$$\frac{D_i(T)}{D_i^{eq}(T)} = \frac{x_v}{x_{v,Al}^{eq}} \tag{20}$$

where $x_{v,Al}^{eq}$ denotes the equilibrium site fraction of vacancy in pure Al. In order to achieve a faster age hardening kinetics, it is important to retain a high density of quenched-in vacancy for AA by optimizing the heat treatment processes and the alloy chemistry.

For the microalloying effect of Sn in Section 4.3, provided that the vacancies which are not trapped by Sn atoms dominate the vacancy-mediated diffusion of precipitate-forming solute atoms [28], it is straightforward to derive the enhancement factor of solute diffusivity by Eq. (20), where x_v should be replaced by $x_{v,rest}$. It can be clearly seen in Fig. 11 that the addition of 100 at. ppm Sn into the 6xxx alloy reduces the solute diffusivity during 1 day of RT storage by a factor of 10, while enhancing that during subsequent AA by a factor of 10 in comparison to the Sn-free alloy. The reason is that Sn atoms can trap excess vacancies at low temperatures and release them again at elevated temperatures. Even though the present model cannot quantitatively reproduce the evolution of precipitation and hardening, the simulated results have caught the main trends revealed in the experimental work [29]. An implementation of the spatial vacancy evolution model into the age hardening precipitation models will significantly improve their predictability, especially on the nucleation and growth kinetics of precipitates. Development of more comprehensive age hardening model considering both atom clustering kinetics and PFZ evolution is in progress.

6. Conclusion

A finite volume numerical model has been developed to simulate the temporal evolution and spatial distribution of non-equilibrium excess vacancies during NA and AA in multicomponent aluminium alloys. In the model, the annihilation mechanisms of vacancies at GBs and dislocations have been rigorously treated while the effect of solute trapping on vacancy evolution has been well addressed. The model has been applied to understand the influences of cooling rate during quenching, NA, temperature of AA, grain size, number density of dislocations and alloy chemistry on the experimentally observed precipitation and age hardening kinetics of heat treatable aluminum alloys. The main concluded remarks are drawn as follows:

(1) The influences of cooling rate of quenching and ageing temperature on the PFZ width in the early stage of AA can be well explained by the spatial distribution of vacancies near the GBs, which is controlled by the GB annihilation of excess vacancies.
(2) The model has been successfully applied to simulate the evolution of excess vacancies under the influences of dislocation density and grain size. The abnormal precipitation behaviors of UFG and nano grained aluminium alloys processed by SPD can be well explained by the rapid annihilation of excess vacancies.
(3) The influences of solute elements, especially Sn, on the evolution of excess vacancies during NA and thereafter on the precipitation kinetics during AA has been quantitatively addressed by considering the trapping effects of solute atoms on vacancies.

Data availability

Data will be made available on request.

Declaration of Competing Interest

The authors declare that they have no known competing financial interests or personal relationships that could have appeared to influence the work reported in this paper.

Acknowledgements

This publication has been funded by the SFI PhysMet, (Centre for Research-based Innovation, 309584). The authors gratefully acknowledge the financial support from the Research Council of Norway and the partners of the SFI PhysMet. The authors also acknowledge the support of the project Fundamentals of Intergranular Corrosion in Aluminium Alloys-FICAL (247598).

Supplementary materials

Supplementary material associated with this article can be found, in the online version, at doi:10.1016/j.actamat.2023.119552.

References

[1] M. Werinos, H. Antrekowitsch, T. Ebner, R. Prillhofer, W.A. Curtin, P. J. Uggowitzer, S. Pogatscher, Design strategy for controlled natural aging in Al–Mg–Si alloys, Acta Mater. 118 (2016) 296–305.

[2] S. Zhu, H.C. Shih, X. Cui, C.Y. Yu, S.P. Ringer, Design of solute clustering during thermomechanical processing of AA6016 Al–Mg–Si alloy, Acta Mater. 203 (2021).

[3] M.D.H. Lay, H.S. Zurob, C.R. Hutchinson, T.J. Bastow, A.J. Hill, Vacancy Behavior and Solute Cluster Growth During Natural Aging of an Al-Mg-Si Alloy, Metall. Mater. Trans. A 43 (12) (2012) 4507–4513.

[4] W. Sun, Y. Zhu, R. Marceau, L. Wang, Q. Zhang, X. Gao, C. Hutchinson*, Precipitation strengthening of aluminum alloys by room-temperature cyclic plasticity, Science 363 (6430) (2019) 972–975.

[5] S. Wu, H.S. Soreide, B. Chen, J. Bian, C. Yang, C. Li, P. Zhang, P. Cheng, J. Zhang, Y. Peng, G. Liu, Y. Li, H.J. Roven, J. Sun, Freezing solute atoms in nanograined aluminum alloys via high-density vacancies, Nat. Commun. 13 (1) (2022).

[6] H. Zhao, F. De Geuser, A. Kwiatkowski da Silva, A. Szczepaniak, B. Gault, D. Ponge, D. Raabe, Segregation assisted grain boundary precipitation in a model Al-Zn-Mg-Cu alloy, Acta Mater. 156 (2018) 318–329.

[7] M. Liu, J. Čížek, C.S.T. Chang, J. Banhart, Early stages of solute clustering in an Al–Mg–Si alloy, Acta Mater. 91 (2015) 355–364.

[8] H. Jia, R. Bjørge, L. Cao, H. Song, K. Marthinsen, Y. Li, Quantifying the grain boundary segregation strengthening induced by post-ECAP aging in an Al-5Cu alloy, Acta Mater. 155 (2018) 199–213.

[9] D. Raabe, D. Ponge, P.J. Uggowitzer, M. Roscher, M. Paolantonio, C. Liu, H. Antrekowitsch, E. Kozeschnik, D. Seidmann, B. Gault, F. De Geuser, A. Deschamps, C. Hutchinson, C. Liu, Z. Li, P. Prangnell, J. Robson, P. Shanthraj, S. Vakili, C. Sinclair, L. Bourgeois, S. Pogatscher, Making sustainable aluminum by recycling scrap: The science of "dirty" alloys, Prog. Mater. Sci. 128 (2022).

[10] A. Deschamps, C.R. Hutchinson, Precipitation kinetics in metallic alloys: Experiments and modeling, Acta Mater. 220 (2021).

[11] L. Bourgeois, Y. Zhang, Z. Zhang, Y. Chen, N.V. Medhekar, Transforming solid-state precipitates via excess vacancies, Nat. Commun. 11 (1) (2020) 1248.

[12] J.D. Embury, R.B. Nicholson, The nucleation of precipitates: The system Al-Zn-Mg, Acta Metall. 13 (4) (1965) 403–417.

[13] P.N.T. Unwin, G.W. Lorimer, R.B. Nicholson, The origin of the grain boundary precipitate free zone, Acta Metall. 17 (11) (1969) 1363–1377.

[14] H. Jiang, R.G. Faulkner, Modelling of grain boundary segregation, precipitation and precipitate-free zones of high strength aluminium alloys—I. The model, Acta Mater. 44 (1996) 1857–1864.

[15] H. Zhao, P. Chakraborty, D. Ponge, T. Hickel, B. Sun, C.H. Wu, B. Gault, D. Raabe, Hydrogen trapping and embrittlement in high-strength Al alloys, Nature 602 (7897) (2022) 437–441.

[16] M.M. Arani, N.S. Ramesh, X. Wang, N. Parson, M. Li, W.J. Poole, The localization of plastic deformation in the precipitate free zone of an Al-Mg-Si-Mn alloy, Acta Mater. 231 (2022).

[17] T.F. Morgeneyer, M.J. Starink, S.C. Wang, I. Sinclair, Quench sensitivity of toughness in an Al alloy: Direct observation and analysis of failure initiation at the precipitate-free zone, Acta Mater. 56 (12) (2008) 2872–2884.

[18] M. Elsayed, T.E.M. Staab, J. Čížek, R. Krause-Rehberg, On the interaction of solute atoms with vacancies in diluted Al-alloys: A paradigmatic experimental and ab-initio study on indium and tin, Acta Mater. 219 (2021).

[19] M. Elsayed, T.E.M. Staab, J. Čížek, R. Krause-Rehberg, Monovacancy-hydrogen interaction in pure aluminum: Experimental and ab-initio theoretical positron annihilation study, Acta Mater. 248 (2023).

[20] Z. Yang, J. Banhart, Natural and artificial ageing in aluminium alloys – the role of excess vacancies, Acta Mater. 215 (2021).

[21] M. Militzer, W.P. Sun, J.J. Jonas, Modelling the effect of deformation-induced vacancies on segregation and precipitation, Acta Metall. Mater. 42 (1) (1994) 133–141.

[22] J.D. Robson, Deformation Enhanced Diffusion in Aluminium Alloys, Metall. Mater. Trans. A 51 (10) (2020) 5401–5413.

[23] F.D. Fischer, J. Svoboda, F. Appel, E. Kozeschnik, Modeling of excess vacancy annihilation at different types of sinks, Acta Mater. 59 (9) (2011) 3463–3472.

[24] J. Svoboda, F.D. Fischer, P. Fratzl, A. Kroupa, Diffusion in multi-component systems with no or dense sources and sinks for vacancies, Acta Mater. 50 (6) (2002) 1369–1381.

[25] J. Svoboda, F.D. Fischer, P. Fratzl, Diffusion and creep in multi-component alloys with non-ideal sources and sinks for vacancies, Acta Mater. 54 (11) (2006) 3043–3053.

[26] J. Svoboda, F.D. Fischer, Vacancy-driven stress relaxation in layers, Acta Mater. 57 (16) (2009) 4649–4657.

[27] F.D. Fischer, J. Svoboda, Substitutional diffusion in multicomponent solids with non-ideal sources and sinks for vacancies, Acta Mater. 58 (7) (2010) 2698–2707.

[28] M.F. Francis, W.A. Curtin, Microalloying for the controllable delay of precipitate formation in metal alloys, Acta Mater. 106 (2016) 117–128.

[29] S. Pogatscher, H. Antrekowitsch, M. Werinos, F. Moszner, S.S. Gerstl, M.F. Francis, W.A. Curtin, J.F. Loffler, P.J. Uggowitzer, Diffusion on demand to control precipitation aging: application to Al-Mg-Si alloys, Phys. Rev. Lett. 112 (22) (2014), 225701.

[30] M. Werinos, H. Antrekowitsch, T. Ebner, R. Prillhofer, P.J. Uggowitzer, S. Pogatscher, Hardening of Al–Mg–Si alloys: Effect of trace elements and prolonged natural aging, Materials & Design 107 (2016) 257–268.

[31] R.W. Balluffi, Mechanisms of Dislocation Climb, Phys. Status Solidi 31 (2) (1969) 443–463.

[32] A. Abu-Odeh, M. Cottura, M. Asta, Insights into dislocation climb efficiency in FCC metals from atomistic simulations, Acta Mater. 193 (2020) 172–181.

[33] J.W. Edington, R.E. Smallman, Faulted dislocation loops in quenched aluminium, The Philosophical Magazine, Philos. Mag. (1798-1977) 11 (114) (1965) 1109–1123.

[34] X. Chen, J.R. Mianroodi, C. Liu, X. Zhou, D. Ponge, B. Gault, B. Svendsen, D. Raabe, Investigation of vacancy trapping by solutes during quenching in aluminum alloys, Acta Mater. 254 (2023).

[35] R.W. Balluffi, S. Allen, W.C. Carter, Kinetics of Materials, Wiley, 2005.

[36] K.L. Baker, W.A. Curtin, Multiscale diffusion method for simulations of long-time defect evolution with application to dislocation climb, J. Mech. Phys. Solids 92 (2016) 297–312.

[37] J. Peng, S. Bahl, A. Shyam, J.A. Haynes, D. Shin, Solute-vacancy clustering in aluminum, Acta Mater. 196 (2020) 747–758.

[38] L. Bukonte, T. Ahlgren, K. Heinola, Thermodynamics of impurity-enhanced vacancy formation in metals, J. Appl. Phys. 121 (4) (2017).

[39] J. Wu, S. Song, A unified model of grain-boundary segregation kinetics, J. Appl. Phys. 110 (6) (2011).

[40] J. Svoboda, F.D. Fischer, Modelling for hydrogen diffusion in metals with traps revisited, Acta Mater. 60 (3) (2012) 1211–1220.

[41] Y. Du, Y.A. Chang, B. Huang, W. Gong, Z. Jin, H. Xu, Z. Yuan, Y. Liu, Y. He, F. Y. Xie, Diffusion coefficients of some solutes in fcc and liquid Al: critical evaluation and correlation, Mater. Sci. Eng. A Struct. Mater. 363 (1-2) (2003) 140–151.

[42] Q.F. Fang, R. Wang, Atomistic Simulation of the Atomic Structure and Diffusion within the Core Region of an Edge Dislocation in Aluminium, Phys. Rev. B 62 (14) (2000) 9317–9324.

[43] E. Clouet, The vacancy–edge dislocation interaction in fcc metals: A comparison between atomic simulations and elasticity theory, Acta Mater. 54 (13) (2006) 3543–3552.

[44] F. Qian, D. Zhao, E.A. Mørtsell, S. Jin, J. Wang, C.D. Marioara, S.J. Andersen, G. Sha, Y. Li, Enhanced nucleation and precipitation hardening in Al–Mg–Si(–Cu) alloys with minor Cd additions, Mater. Sci. Eng. A Struct. Mater. 792 (2020).

[45] P. Gay, P.B. Hirsch, A. Kelly, The estimation of dislocation densities in metals from X-ray data, Acta Metall. 1 (3) (1953) 315–319.

[46] D. Caillard, J.L. Martin, Pergamon Materials Series, Thermally Activated Mechanisms in Crystal Plasticity, 2003.

[47] U. Messerschmidt, Dislocation Dynamics During Plastic Deformation, Springer Berlin, Heidelberg, 2010.

[48] C.D. Marioara, A. Lervik, J. Grønvold, O. Lunder, S. Wenner, T. Furu, R. Holmestad, The Correlation Between Intergranular Corrosion Resistance and Copper Content in the Precipitate Microstructure in an AA6005A Alloy, Metall. Mater. Trans. A 49 (10) (2018) 5146–5156.

[49] J. Svoboda, Y.V. Shan, E. Kozeschnik, F.D. Fischer, Couples and pairs formation—thermodynamic and kinetic modelling applied to Al–Mg–Si, Modell. Simul. Mater. Sci. Eng. 25 (6) (2017).

[50] C.D. Marioara, T. Børvik, O.S. Hopperstad, The relation between grain boundary precipitate formation and adjacent grain orientations in Al-Mg-Si(-Cu) alloys, Philos. Mag. Lett. 101 (9) (2021) 370–379.

[51] A.B. Hagen, S. Wenner, R. Bjørge, D. Wan, C.D. Marioara, R. Holmestad, I. G. Ringdalen, Local mechanical properties and precipitation inhomogeneity in large-grained Al-Mg-Si alloy, Mater. Sci. Eng. A Struct. Mater. (2022).

[52] Y. Huang, J.D. Robson, P.B. Prangnell, The formation of nanograin structures and accelerated room-temperature theta precipitation in a severely deformed Al–4wt.% Cu alloy, Acta Mater. 58 (5) (2010) 1643–1657.

[53] W. Lechner, W. Puff, B. Mingler, M.J. Zehetbauer, R. Würschum, Microstructure and vacancy-type defects in high-pressure torsion deformed Al–Cu–Mg–Mn alloy, Scr. Mater. 61 (4) (2009) 383–386.

[54] P. Dumitraschkewitz, P.J. Uggowitzer, S.S.A. Gerstl, J.F. Loffler, S. Pogatscher, Size-dependent diffusion controls natural aging in aluminium alloys, Nat. Commun. 10 (1) (2019) 4746.

[55] O.R. Myhr, Ø. Grong, Modelling of non-isothermal transformations in alloys containing a particle distribution, Acta Mater. 48 (7) (2000) 1605–1615.

[56] M. Nicolas, A. Deschamps, Characterisation and modelling of precipitate evolution in an Al–Zn–Mg alloy during non-isothermal heat treatments, Acta Mater. 51 (20) (2003) 6077–6094.

[57] D. Bardel, M. Perez, D. Nelias, A. Deschamps, C.R. Hutchinson, D. Maisonnette, T. Chaise, J. Garnier, F. Bourlier, Coupled precipitation and yield strength modelling for non-isothermal treatments of a 6061 aluminium alloy, Acta Mater. 62 (2014) 129–140.

[58] J.D. Robson, M.J. Jones, P.B. Prangnell, Extension of the N-model to predict competing homogeneous and heterogeneous precipitation in Al-Sc alloys, Acta Mater. 51 (5) (2003) 1453–1468.

[59] D. Zhao, Y. Xu, S. Gouttebroze, J. Friis, Y. Li, Modelling the Age-Hardening Precipitation by a Revised Langer and Schwartz Approach with Log-Normal Size Distribution, Metall. Mater. Trans. A 51 (9) (2020) 4838–4852.

[60] M. Bignon, P. Shanthraj, J.D. Robson, Modelling dynamic precipitation in pre-aged aluminium alloys under warm forming conditions, Acta Mater. 234 (2022).

[61] C.R. Hutchinson, F. de Geuser, Y. Chen, A. Deschamps, Quantitative measurements of dynamic precipitation during fatigue of an Al–Zn–Mg–(Cu) alloy using small-angle X-ray scattering, Acta Mater. 74 (2014) 96–109.

[62] M.A. van Huis, M.H.F. Sluiter, J.H. Chen, H.W. Zandbergen, Concurrent substitutional and displacive phase transformations in Al-Mg-Si nanoclusters, Phys. Rev. B 76 (17) (2007).
[63] S.J. Andersen, C.D. Marioara, J. Friis, S. Wenner, R. Holmestad, Precipitates in aluminium alloys, Adv. Phys. X 3 (1) (2018).
[64] M. Mantina, Y. Wang, L.Q. Chen, Z.K. Liu, C. Wolverton, First principles impurity diffusion coefficients, Acta Mater. 57 (14) (2009) 4102–4108.